

## ACTIVE REGION LOOPS OBSERVED WITH SUMER ON BOARD THE *SOLAR AND HELIOSPHERIC OBSERVATORY*

JONGCHUL CHAE, HAIMIN WANG, JIONG QIU, AND PHILIP R. GOODE

Big Bear Solar Observatory, New Jersey Institute of Technology, 40386 North Shore Lane, Big Bear City, CA 92314-9672; chae@bbso.njit.edu

AND

KLAUS WILHELM

Max-Planck-Institut für Aeronomie, D-37191 Katlenburg-Lindau, Germany

Received 1999 June 7; accepted 1999 November 30

### ABSTRACT

We study the emission and dynamical characteristics of transition region temperature plasmas in magnetic loops by analyzing a high-resolution, limb observation of the active region NOAA 7962. The observations were performed by the Solar Ultraviolet Measurements of Emitted Radiation (SUMER) instrument on board the *Solar and Heliospheric Observatory (SOHO)*. The SUMER observation produced a set of raster scans of the region, in the four lines, H I Ly $\beta$   $\lambda$ 1025, O VI  $\lambda$ 1032, 1038, and C II  $\lambda$ 1037. The data are used to construct intensity, velocity, and line width maps of the active region, from which more than 10 well-resolved loops are identified and classified into four different groups. We determine several physical parameters of the loops in each group such as diameter, length, temperature, line-of-sight plasma velocity, and nonthermal line broadening. Our results indicate that both kinds of temperature variations exist in active region loops: variations from loop to loop and variations along each loop. It is also found that there is a distinction between stationary loops and dynamic loops. The dynamic loops have large bulk motions and large nonthermal line broadenings. Some of the dynamic loops display large velocity shears with the sign of line-of-sight velocities changing across the loop axes. These velocity shears appear to represent rotational motions around the loop axes with velocities of up to 50 km s<sup>-1</sup>. There are indications that nonthermal line broadening is the result of magnetohydrodynamic turbulence inside the loops. Based on our observations, we postulate that when loops erupt, some of the kinetic and magnetic energy cascades down to turbulent energy which would be dissipated as heat.

*Subject headings:* MHD — Sun: flares — Sun: transition region — Sun: UV radiation

### 1. INTRODUCTION

Observations have revealed that magnetic loops are a basic component of the magnetized outer solar atmosphere. Daily images of the Sun and the corona are available from recent experiments such as *Yohkoh* Soft X-ray Telescope (SXT), the Extreme-Ultraviolet Imaging Telescope (EIT) on the *Solar and Heliospheric Observatory (SOHO)*, and the *Transition Region And Coronal Explorer (TRACE)*. They clearly demonstrate that the outer solar atmosphere is pervaded by loops of different sizes (ranging in length from 10<sup>4</sup> to several times 10<sup>5</sup> km) producing predominant emissions at different wavelengths such as ultraviolet (UV), extreme-ultraviolet (EUV), and X-ray. Most of the prominent loops are found in active regions, but loops are often observed outside active regions, too. Therefore, investigating magnetic loops is essential to understand the mysteries of heating, mass supply, and acceleration in the Sun's outer atmosphere.

Not surprisingly, our knowledge on magnetic loops has increased with the sophistication of observing techniques—especially the improvement of spatial resolution and the availability of simultaneous multiwavelength observations. Recently, several interesting results were obtained from the observations of the Coronal Diagnostic Spectrometer (CDS) on *SOHO*. For example, Fludra et al. (1997) and Matthews & Harra-Murnion (1997) found that plasmas with different temperatures exist in different loops. On the other hand, Kjeldseth-Moe & Brekke (1998) provided counterexamples that show the co-location of multi-

temperature plasmas within the resolution of CDS. These apparently contradicting results should be resolved from higher resolution observations. Meanwhile, CDS observations have displayed many O VI loops with well-defined cross sections that intrude into the hotter corona. The plasma in these loops often emits lines that are strongly Doppler-shifted (Brekke, Kjeldseth-Moe, & Harrison 1997), which implies that the loops are not static. That O VI loops undergo dynamic evolutions, like outward expansion, was directly demonstrated with CDS movies of O VI images (Kjeldseth-Moe & Brekke 1998; Brekke 1998). Note that this dynamic behavior of O VI loops is very similar to the outward expansion of much hotter X-ray loops as is well known from *Yohkoh* Soft X-ray observations (Uchida et al. 1992).

Some important questions emerge from these recent results: Do magnetic loops also have significant temperature variations inside or along the loops in addition to the variations from loop to loop? Are loops of different temperatures causally connected via cooling or heating? If so, how does thermal evolution occur? Is thermal evolution related to dynamical evolution? To search for answers to these questions, we study active region loops seen in UV lines at the limb using observations of the Solar Ultraviolet Measurements of Emitted Radiation (SUMER) instrument on board *SOHO*. Note that the present study is confined to transition region temperatures since the lines used are emitted from plasmas at  $T < 5 \times 10^5$  K. SUMER has a higher spatial resolution and spectral resolution than CDS,

and should be well suited to study loop dynamics as well as emission characteristics. Regrettably, it is not dedicated to the study of active regions. It has often avoided pointing at active regions to protect its detectors. As a result, there are not many SUMER observations of active regions, whereas it has produced an enormous amount of quiet Sun data. This paper describes an exceptional SUMER observation of an active region at the limb where a small (B-class) flare occurred during the observation. This provides one of the few very good opportunities to use SUMER for a detailed study of active region loops at transition region temperatures, especially in relation to a small flare.

In the following, we classify loops based on their thermodynamic and dynamical characteristics. We also derive the physical parameters of the resolved loops, such as length, shape, diameter, temperature, bulk motion, and nonthermal line broadening, which may be useful to constrain theoretical modelings of loop structures and dynamics as well as to answer the questions raised above.

## 2. OBSERVATION AND DATA ANALYSIS

### 2.1. Observation

The active region NOAA 7962 was observed by SUMER on 1996 May 6 when it was at the east limb. A raster scan was made from east to west with 7.5 s exposure time and a  $0''.76$  step size. It started at 13:40 UT and ended at 14:00 UT covering an area of  $120'' \times 120''$ . Figure 1 compares the spatial and temporal coverage of the SUMER observation with a *Yohkoh* full-disk image and *GOES* low-energy band X-ray data. The characteristics and performance of the SUMER instrument were fully described by Wilhelm et al. (1995, 1997) and Lemaire et al. (1997). The selected spectral band includes the H I Ly $\beta$ , O VI  $\lambda\lambda 1032, 1038$ , and C II  $\lambda 1037$  lines. At these wavelengths, the spectral dispersion is about 44 mÅ per detector pixel. Detector "A" was used to record the spectra. Since active regions emit intense UV radiation, the narrow and short ( $0''.3 \times 120''$ ) slit "6" at the top portion of the detector was chosen to protect the detector. For the same reason, the strong Ly $\beta$  and O VI  $\lambda 1032$  lines were set to be recorded on the less sensitive bare part of the detector. The spatial resolution (FWHM) of the SUMER observations is known to be better than  $1''$  across and about  $1''.5$  along the slit direction (Lemaire et al. 1997).

The spectral resolution (FWHM) is about 2.3 detector pixels according to Chae, Schühle, & Lemaire (1998a), which corresponds to 100 mÅ or  $29 \text{ km s}^{-1}$ , respectively, at the chosen spectral band. Note that it is possible to determine line positions to much higher precision than this, that is, to  $1\text{--}2 \text{ km s}^{-1}$ , when line fitting techniques are applied to high signal-to-noise ratio data (see, e.g., Chae, Yun, & Poland 1998b).

### 2.2. Data Reduction

The data reduction procedures consist of corrections for gain variation, saturation, and geometric distortion of the detector. The correction for the gain variations across the detector has been done using the long-integration flat image obtained on 1996 May 15. Since there was a nine day gap between our observations and the flat image observation, the gain pattern may have changed during the interval, and this may lead to an uncertainty in the gain correction. According to Chae et al. (1998b), the gain pattern changes over several days in a more or less random way. As a result, an additional random noise is introduced in each detector pixel which is proportional to the signal count at the corresponding pixel. Chae et al. (1998b) found that this kind of noise may introduce a random error in the Doppler shift measurement of about  $1 \text{ km s}^{-1}$ . We regard this amount of error tolerable for our study. More serious may be the imperfections in the gain variation correction on some specific detector portions which have significant defects. It may produce nonnegligible systematic errors in the determinations of Doppler shifts and line widths, as well as line intensities. Note that this kind of error is easily identified from raster images, since they produce stripe patterns in the direction perpendicular to the slit.

Next, the data are corrected for the detector dead-time effect and local gain depression using the standard SUMER correction routines. We find that count data in most portions of the observed loops above the limb have been little saturated, but those in the small flaring area and the regions very close to the limb have been too saturated to be used for quantitative analyses.

Another important part of the data reduction is the correction for the geometric distortion of the detector, which is due to the displacement of photon-event positions on the

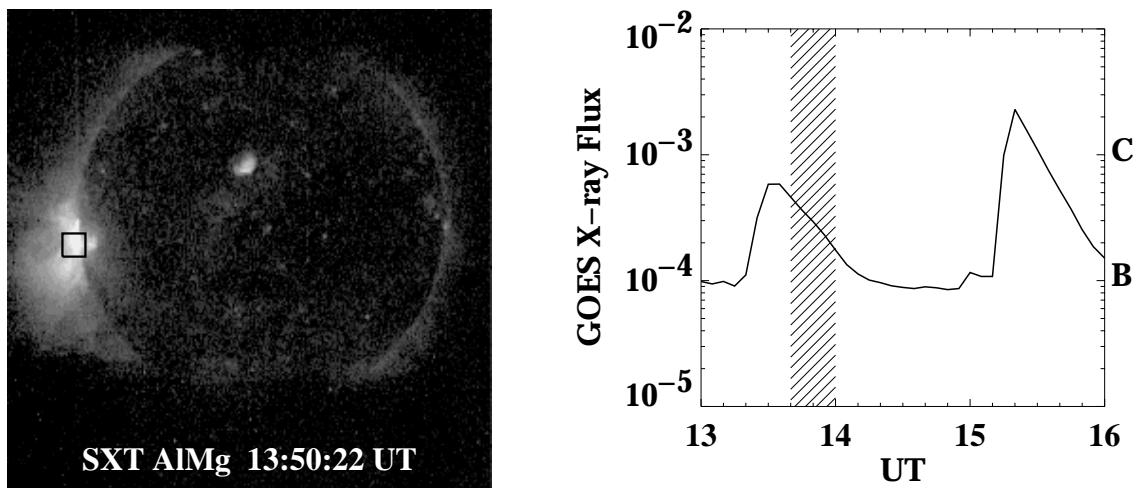


FIG. 1.—Spatial and temporal coverage of the SUMER observation on 1996 May 6 as compared with a *Yohkoh* full disk image (box, left) and *GOES* low-energy band X-ray data (hatched area, right).

detector plane. There are two kinds of distortions: One is distortion across the slit that affects the spectral positions of photon events and, hence, spectral calibrations of Doppler shifts. The other is the distortion along the slit that affects the spatial positions of emission sources and, hence, raster images. For the correction of spectral distortions, we employed the method of two-dimensional mapping that has been described in detail by Chae et al. (1998b). This method uses the calibration data provided by T. Moran and is basically the same as his routine except that it has been adapted to speed up the computation. We checked the precision of the corrections by examining the spatial variation along the slit of the spectral positions of the O VI  $\lambda 1038$  line which were determined from the corrected data in the first few rasters. Since these rasters cover altitudes very high above the solar limb, most of the O VI emissions may come from the stationary diffusive hot corona, and therefore the line positions should not change systematically along the slit if the geometric distortion correction has been properly done. The systematic change of the line position is found to be less than  $2 \text{ km s}^{-1}$ , indicating that the distortion correction is good enough for our purpose.

For the correction of spatial distortions along the slit, we have tried to use the standard calibration data as well. However, the results were not satisfactory. Even after the corrections, there remained nonnegligible amounts of relative displacements between the emission features in the two O VI lines that supposedly display the common emission features. Therefore, we followed a different approach that makes use of the emission features that are commonly seen in different lines. The emission features in the C II  $\lambda 1037$  and O VI  $\lambda 1038$  lines are used as references. We neglect the relative spatial displacements between the emission features of these two lines, since they are close enough to each other on the detector (Moran's data imply that these two lines should be spatially co-located within  $0''.5$ ). To correct for the spatial distortions in Ly $\beta$ , we identified the Ly $\beta$  counterparts of the C II emission features by comparing the two raster images that were constructed without correcting for spatial distortions. Systematic displacements of  $3''$ – $7''$  were found between the emission features of the two lines. These values are larger than the values of about  $2''$  implied from the standard calibration data. We do not know the cause of this difference. The derived displacements of Ly $\beta$  features have been used to destretch the Ly $\beta$  line data along the slit. Following the same procedure, the O VI  $\lambda 1032$  line data also have been destretched along the slit direction with respect to the O VI  $\lambda 1038$  data. The required amount of destretching was about  $2''$ . The precision of geometrical corrections along the spatial direction has been examined by comparing the intensity images which were constructed from distortion-corrected data. It is found that displacements are usually within  $1''$ , the size of a spatial element.

### 2.3. Spectral Analysis

We have determined the line parameters (continuum level, peak intensity, line position, and line width) for the two O VI lines and the Ly $\beta$  line at every spatial point, by applying single Gaussian fittings to the spectral data. We used a nonlinear least-squares fitting method described by Chae et al. (1998b). The set of line parameters at every point were then used to estimate the integrated line intensity  $I$ , the Doppler shift  $v$ , and the Doppler width  $v_D$ . It is straightforward to obtain the integrated line intensity in unit of counts

per spatial element from the peak intensity and line width. The radiometric calibration is then performed using the standard SUMER routine to determine the line intensity in physical units,  $\text{ergs cm}^{-2} \text{ s}^{-1} \text{ sr}^{-1}$ .

The determination of the Doppler shift  $v$  (in  $\text{km s}^{-1}$ ) from the measured position  $x$  (in pixels) of a line requires knowing the rest position  $x_0$  of the line emitted by the stationary plasma. In the case of the O VI lines, we simply took the spatial averages of the line positions over the rasters covering the diffusive hot corona. For the Ly $\beta$  line, the coronal emissions are too weak to allow the meaningful determination of the line positions at each spatial element. So, we first took the spatial average of the line profiles over an area of  $5'' \times 10''$  centered at each spatial point and determined the line position at that point. Then we took the spatial average of the line positions over the rasters covering the diffusive hot corona. Once the rest position of every line is determined, it is straightforward to determine the Doppler shift  $v$  in units of  $\text{km s}^{-1}$  from the measured line position at every point using the known spectral dispersion value  $d\lambda/dx$

$$v = (x - x_0) \frac{d\lambda}{dx} \frac{c}{\lambda}. \quad (1)$$

Note that this method of determining Doppler shifts is insensitive to the used spectral dispersion  $d\lambda/dx$  and rest wavelength  $\lambda$ . Using this method, we obtained the average Doppler shifts over the last 10 rasters which cover the disk area  $30''$  inside the limb. They are redshifted and have the values  $7.3 \text{ km s}^{-1}$  for the O VI  $\lambda 1032$  line,  $7.8 \text{ km s}^{-1}$  for the O VI  $\lambda 1038$  line, and  $1.9 \text{ km s}^{-1}$  for the Ly $\beta$  line, respectively. These values can be compared with the quiet Sun disk center Doppler shift values of  $8.7 \text{ km s}^{-1}$  for the O VI ions and  $2.6 \text{ km s}^{-1}$  for the Si II ions measured by Chae et al. (1998b) using chromospheric lines as references. It is interesting that the two sets of Doppler shifts determined using different methods produce similar values despite the different observing areas.

The determination of the Doppler width  $v_D$  (in  $\text{km s}^{-1}$ ) from the measured Gaussian width  $\sigma_x$  (in unit of pixels) of a line is easily done correcting for the instrumental broadening  $\sigma_I$

$$v_D = \sqrt{2(\sigma_x^2 - \sigma_I^2)} \frac{d\lambda}{dx} \frac{c}{\lambda}. \quad (2)$$

We have adopted 2.3 detector pixels for the FWHM value of the instrumental width as determined by Chae et al. (1998a), which corresponds to  $\sigma_I = 0.98$  pixel.

Once the line parameters are determined at every spatial element, they are used to construct line intensity, Doppler shift, and Doppler width maps of the observed region in each line. These maps are useful in examining the emission and dynamical characteristics of the observed area, at least for qualitative purposes. For quantitative studies, however, one should be careful in using the values presented in the raster image data, since they have been derived from the original spectral data, based on the simple assumption that the spectral lines are well fitted by single Gaussians. There are several factors that may make the use of single Gaussian fittings inadequate for quantitative studies. One is detector saturation at very bright regions such as the flaring region and the regions very close to the limb. We have not attempted to analyze the spectral data in these regions.

Another factor to be considered is the self-reversal feature seen in the core of Ly $\beta$  line profiles. This is a consequence of non-LTE radiative transfer in the line and is prominent in the regions close to, or inside the limb. In these regions, both the Doppler velocity and the Doppler width, which have been determined from single Gaussian fits, are questionable. At regions far outside of the limb, the line profiles are not self-reversed so that the Doppler velocity can be fairly well determined. But the interpretation of the Doppler width is not simple because the broadening due to the opacity effect still dominates the Ly $\beta$  line. Therefore, our use of the Ly $\beta$  data is mostly limited to looking at the Ly $\beta$  emission features in the observed area and examining the Doppler shift characteristics of loops at  $T < 10^5$  K.

Finally, the emissions from the diffuse hot corona are not negligible in the O VI line profiles as inferred from the high-temperature tail in the O VI ionization equilibrium curve. Thus, the measured O VI line emissions should be considered to be the superposition of emissions from cool transition region plasmas in magnetic loops and the diffuse hot coronal plasma located along the line of sight. The coronal emissions should be subtracted from the line profiles for the proper evaluation of emission and dynamical characteristics of transition region plasmas in magnetic loops. We will deal with this problem in the next section.

### 3. RESULTS

#### 3.1. Identification and Classification

Figure 2 compares integrated line intensity images of the observed area in the four lines. The direct integration method has been used to determine the intensities in the lines since the C II line is not strong enough to allow the line fitting at every spatial point. The loop system looks similar in the two O VI lines and in the C II and Ly $\beta$  lines, but there are many differences between the structures seen in these two groups. Note also that some Ly $\beta$  loops are barely visible in the C II line.

Figure 3 shows the intensity maps of the active region constructed by applying a single Gaussian fit to the O VI  $\lambda 1038$  and Ly $\beta$  line data at every spatial point. The intensity images in Figure 3 are practically the same as the corresponding ones in Figure 2, demonstrating that direct integration and Gaussian fitting produce the same results, as far as the intensities of these lines are concerned. We have not presented in these figures the raster images of the O VI  $\lambda 1032$  line since they supposedly display the same features as the other O VI line. We have not included the images of

the C II  $\lambda 1037$ , either, since the line is too weak in many spatial elements to allow us to determine the line parameters at those points in a reasonable way.

From the raster images, we identified more than 10 resolved loop and marked them on the figures with annotated dotted curves. Depending on their shapes, inclinations, and visibilities, the loops may be categorized into four groups. The first (I) group consists of the closed loops that are clearly visible in all the lines: loops 1, 2, 3, and 11 belong to this group. In the present study, “closed” loops mean the loops where both footpoints can be seen inside the field of view whereas “open” loops refer to the other structures. Thus, observed “open” loops may represent only the visible parts of large loops most parts of which may be invisible, irrespective of whether they are really open or not. The second (II) group consists of the “open” loops, which are highly inclined to the vertical, and clearly visible in the Ly $\beta$  and C II lines but much fainter in the O VI line: loops 4 and 5 belong to this group. The third (III) group includes loops 6, 7, and 8, which are clearly visible in the O VI lines but are very weak in the C II line. These loops appear open and almost vertical. Finally, the fourth (IV) group contains loops 9 and 10. As far as their shape and visibility are concerned, these loops look similar to the loops in group III but appear to have larger diameters and to be much more dynamic than group III loops. There may be a few more loops visible in the same field of view, but we do not consider them in the present study since they appear relatively incomplete.

The above classification is intended mainly for an ordering of observations and for seeking the answers to the questions raised in the introduction. Nevertheless, it is also useful in demonstrating that there are variations of temperatures, geometries, and dynamical characteristics from loop to loop at transition region temperatures.

#### 3.2. Diameters and Lengths

We define a loop diameter,  $d$ , by the FWHM of the intensity distribution across the loop. Loop diameters are derived from the intensity maps of the O VI  $\lambda 1038$  and C II  $\lambda 1037$  lines, since these lines are subject to relatively small geometric distortion. After subtracting the instrumental blurring (which is about 1" across and 1/5 along the slit direction) from the measured diameters, we obtain about the same diameter of 1400 km in the C II line for loops 3 and 4. This value is not much different from that of loop 3 determined in the O VI line. The diameters of loops 7, 8, and

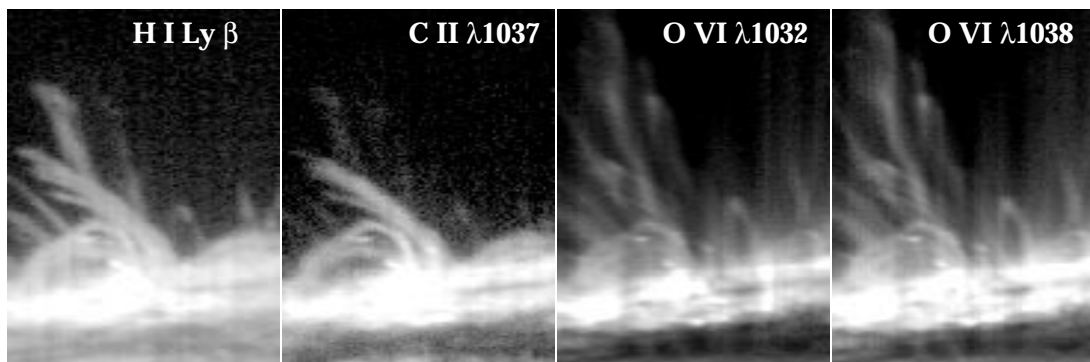


FIG. 2.—Raster images of the active region constructed for the four different lines. The solar east is up, and the north is on the right side. The slit is oriented in the north-south direction.

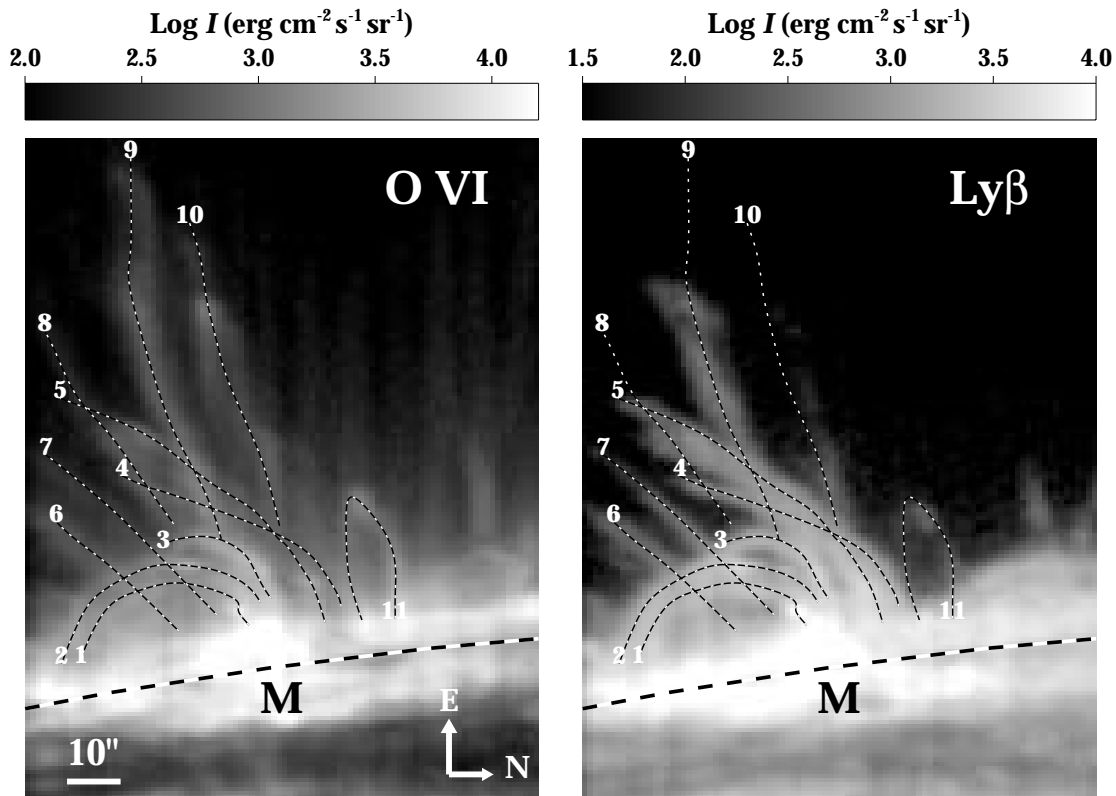


FIG. 3.—Integrated line intensity maps of the active region constructed from the O VI  $\lambda 1038$  (left) and Ly $\beta$  line (right) raster scan data, respectively. The dashed curves represent the location of the white light limb. The identified loops are represented by the dotted curves with the annotating numbers.

12 are determined to be 1300, 2100, and 1700 km in the O VI line, respectively. Summing up, the loops that belong to groups I–III have diameters in the range 1000–2000 km. There is no indication that the diameters of these loops vary significantly along the loops. Note, however, that this applies to the higher portions of the loops which are clearly visible in the present data. The diameters near the footpoints are difficult to measure because of the crowded overlapping. Loops 9 and 10 in group IV have larger diameters than the other loops. These loops have relatively ill-defined shapes and irregularly varying diameters. The determined diameter of loop 9 ranges from 2400 to 2800 km, that of loop 10 from 2100 to 3300 km.

The determination of loop length,  $L$ , is affected by the projection effect and the limited visibility of the loop. Determining the lengths of the loops belonging to group I is relatively easy since they display well-defined closed shapes. The footpoint separation of, for example, loop 2 is about  $2.5 \times 10^4$  km, the top height is about  $1.5 \times 10^4$  km, and the loop length is about  $5.0 \times 10^4$  km without taking into account the projection effect. The other closed loops 1, 3, and 11 may have loop lengths comparable to these values. It is difficult to determine the lengths of the “open” loops in groups II, III, and IV, since substantial parts are invisible. The actual loop lengths might be much more than twice the length of the visible parts. Thus we get only the lower bounds of the loop lengths, which are  $(8\text{--}14) \times 10^4$  km.

### 3.3. Temperature Variations

Since the Ly $\beta$ , C II, and O VI lines are formed at different temperatures, the relative visibilities of the loops in these lines allow us to infer temperatures of the loop plasmas.

According to the ionization equilibria of Arnaud & Rothenflug (1985), the C II and O VI ion abundances have their peaks around  $2.5 \times 10^4$  K and  $3.0 \times 10^5$  K, respectively. Since each line is emitted by plasmas with a range of temperature rather than a single temperature, it would be conservative to mention that the C II line is formed by plasma with  $T_e < 10^5$  K whereas the O VI line, by plasma with  $T_e > 10^5$  K. The Ly $\beta$  line seems to have a broader range of formation temperature than the C II line, possibly covering temperatures of up to  $10^5$  K as inferred from Figure 2.

The examination of the relative visibilities of the loops in the different lines indicates that the temperature may vary along each loop as well as from loop to loop. Loops 4 and 5 in group II appear to be the coolest ( $T_e < 10^5$  K) since they are clearly visible in the Ly $\beta$  and C II lines but not visible in the O VI data. A careful examination also reveals that the C II visibility decreases with height along the loops whereas the O VI visibility is enhanced at the upper portions. This may suggest that the temperature increases with height along the loops. Loops 1, 2, and 3 in group I are visible in all the lines with the relative visibilities depending on the position along the loops. Thus, they seem to have a mixture of cool ( $T_e < 10^5$  K) and hot ( $T_e > 10^5$  K) plasma. The other loops 6, 7, 8, 9, and 10 in groups III and IV are clearly visible in the O VI lines but are very faint in the C II line. Consequently, they appear to be hotter ( $T_e > 10^5$  K). These loops also display changes of intensities with height. In Ly $\beta$ , only the lower portions of these loops are clearly visible, whereas the O VI lines show both the upper and lower portions. Therefore, like group II loops, group III and IV loops also seem to have higher temperatures in their upper portions.

### 3.4. Bulk Motions

Figure 4 shows the line-of-sight velocities of the active region loops. Note that the spatial averages of the line-of-sight velocities over the area far outside the limb have been taken to be zero as the reference. Loops 1, 2, and 3 in group I display large Doppler shifts in the parts near the bright area M (see Fig. 3). Redshifts of up to  $20 \text{ km s}^{-1}$  (O VI) and  $35 \text{ km s}^{-1}$  ( $\text{Ly}\beta$ ) are found in loop 2, and blueshifts of up to  $14 \text{ km s}^{-1}$  (O VI and  $\text{Ly}\beta$ ) are found in loops 1 and 3. Loops 4 and 5 in group II do not display any noticeable line-of-sight velocities in the O VI and  $\text{Ly}\beta$  lines. Thus, these loops appear to be rather stationary. Loop 7 in group III does not display any significant line-of-sight velocity, either, while loop 8 in the same group shows blueshifts of  $12 \text{ km s}^{-1}$ .

Loops 9 and 10 in group IV appear to be different from other loops in that they show large Doppler shifts all along the loops. Loop 9 displays redshifts of about  $20 \text{ km s}^{-1}$  in the O VI line. In loop 10, redshifts of about  $25 \text{ km s}^{-1}$  are found from the  $\text{Ly}\beta$  line. Since a line-of-sight velocity represents only one component of the three-dimensional full velocity vector, the total speed of bulk motion must be larger than these values. It is difficult to imagine in which direction the full velocity vectors are oriented, due to lack of information of the other two components. Nevertheless, it is likely that the velocity vectors have significant components perpendicular to the loop axis, since the loops seen at the limb are directed more or less perpendicular to the line of sight. Therefore, these loops might be under eruption or expansion which is characterized by the existence of mass motion perpendicular to the loop axes. If so, the loop eruptions would produce distortions in the shapes of the loops in the raster maps because of displacements of the loops

occurring during the raster scan. In fact, we see from Figures 3–6 below that loops 9 and 10 look slightly irregular when compared with other loops, indicating some distortions. Particularly, loop 10 seems to have a misalignment between the upper and lower portions, with an offset of a few arcseconds. Note that the upper and lower portions were observed at different times with an interval of a few minutes. The offset could be easily explained by assuming a northward displacement with a velocity of  $25 \text{ km s}^{-1}$ , which is comparable to the observed line-of-sight velocities. The velocities appear to be rather small compared with the known typical velocity in eruptions of  $100 \text{ km s}^{-1}$  or higher. Possibly we are looking at the loops in a late stage of eruption.

Figure 4 also shows that loops 9 and 10 have large variations in line-of-sight velocities across the loops. This kind of velocity shear is prominent at the cut  $R_1$  from the O VI data in loop 10, and at the cut  $R_2$  from the  $\text{Ly}\beta$  data in loop 9. Figure 5 shows the spectrograms, and the profiles of intensity and Doppler velocity at these cuts. It is clear from the figure that both of the spectrograms are tilted with respect to the spatial direction at  $R_1$  and  $R_2$ . Similar tilts have been reported in the H $\alpha$  spicules at the limb and are interpreted as evidence for rotational motions around spicules (e.g., Beckers 1972). If the observed velocity shear is caused by rotational motions, the rotational velocity at  $R_1$ , as seen in the O VI lines, is about  $13 \text{ km s}^{-1}$  and that at  $R_2$ , as seen in the  $\text{Ly}\beta$  line, is about  $45 \text{ km s}^{-1}$ .

There is a small problem in interpreting the velocity shears as rotational motions. Figure 4 shows that the O VI line does not display noticeable blueshift in loop 9 unlike the  $\text{Ly}\beta$ . This is difficult to understand but might in part be

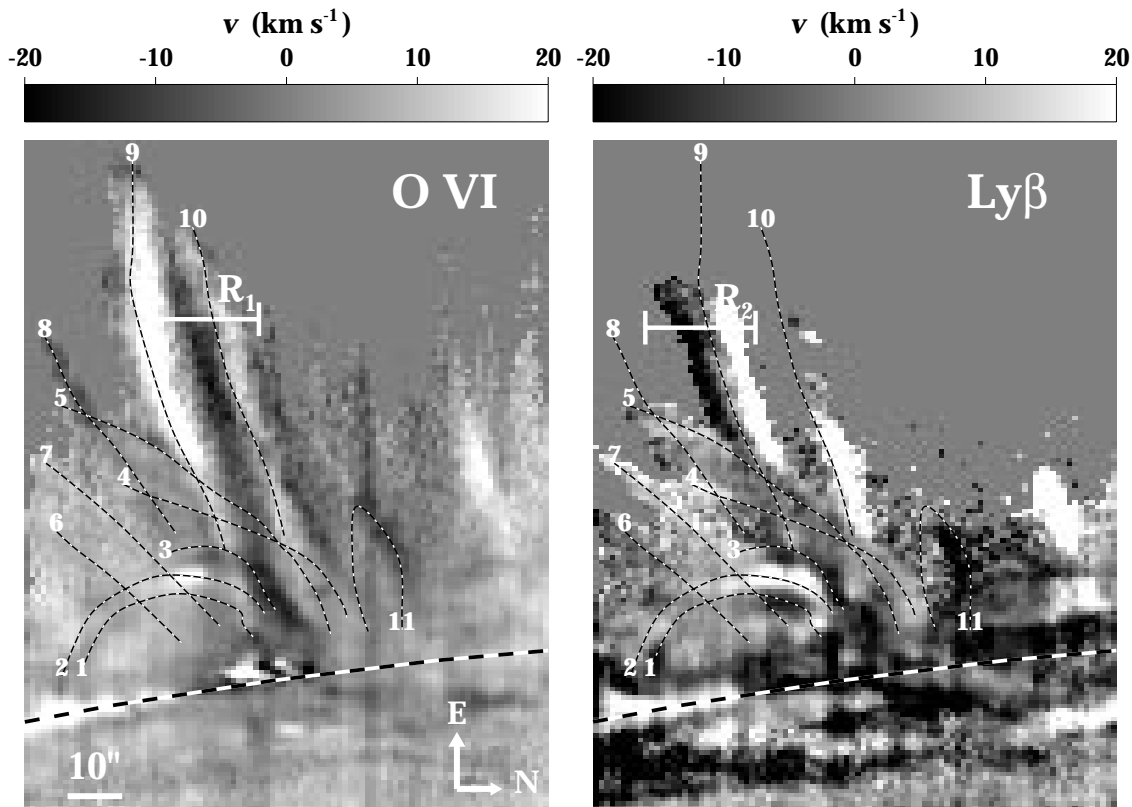


FIG. 4.—Doppler velocity maps of the active region in the O VI line (left) and the  $\text{Ly}\beta$  line (right). The bright features are redshifted and the dark features, blueshifted. Note the large velocity shears at the cuts  $R_1$  and  $R_2$ .

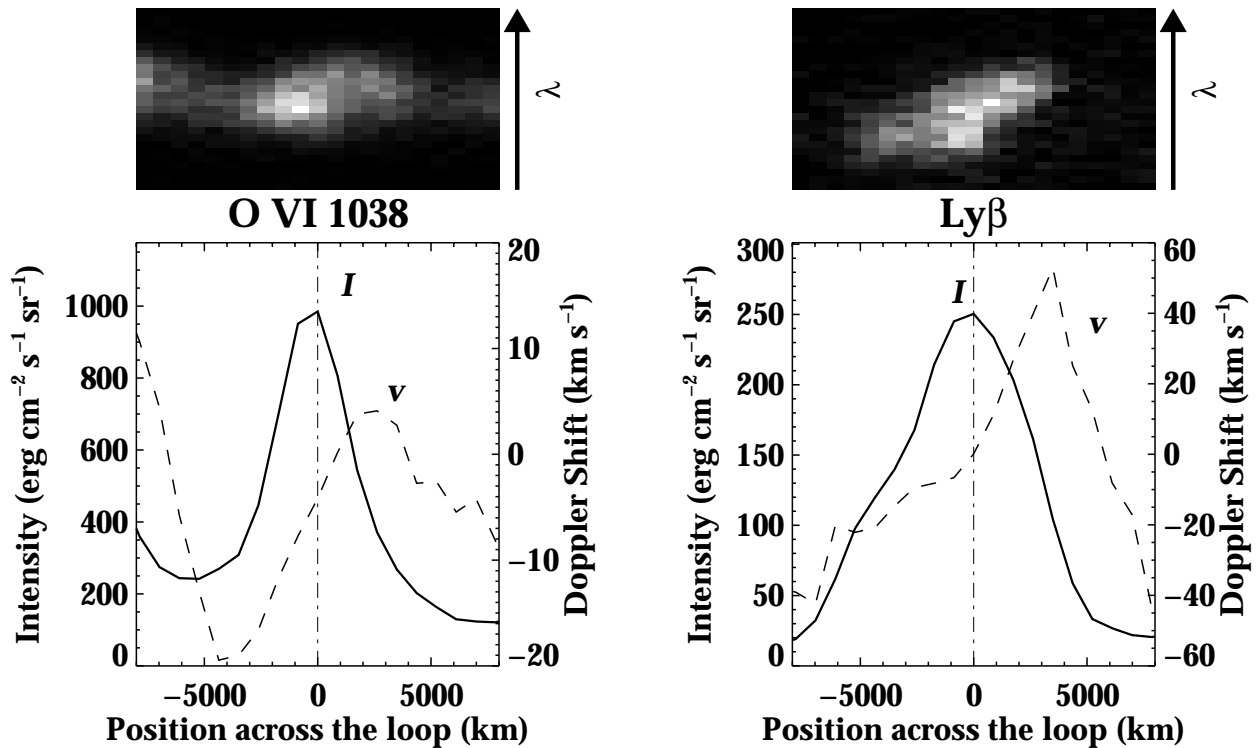


FIG. 5.—Left: O VI spectrogram at the cut  $R_1$  in Fig. 4 (top) and the integrated intensity and Doppler velocity profiles of the same line along the same cut (bottom). Right: Ly $\beta$  spectrogram at the cut  $R_2$  in Fig. 4 (top) and the integrated intensity and Doppler velocity profiles of the same line along the same cut (bottom).

due to the fact that the stationary coronal background contamination has not been corrected in deriving the O VI Doppler shift map. Our examination of the O VI line spectrograms reveal that the O VI line is also tilted at loop 9, indicating that the loop may have rotational motion in the O VI data.

Another possible explanation of the different velocity pattern of loop 9 in the O VI and Ly $\beta$  lines could be a partial overlap of two adjacent loops. Suppose that loop 9 actually consists of two loops: one strongly redshifted at the right side and the other strongly blueshifted at the left side. If the left blueshifted loop is too cool to be visible in the O VI line, then the O VI line would display the right redshifted loop predominantly. This interpretation satisfactorily explains the O VI velocity pattern of loop 9, but a special condition is required for the same interpretation to explain the Ly $\beta$  velocity pattern. It is easy to explain the left blueshifted part of loop 9 seen in Ly $\beta$  since it might be contributed by the assumed blueshifted cool loop at the left side. But it is hard to explain the right redshifted part in a similar way, since the assumed hot loop at the right side should have a temperature suitable to produce strong emissions of both the O VI and Ly $\beta$  lines. An easier explanation may be that the entire Ly $\beta$  emission may come from a cool loop which has rotational motion around its own axis. In conclusion, even if there is ambiguity in the interpretation of the observed emission characteristic, the velocity shear of loop 9 seen in Ly $\beta$  seems in any case to represent the rotational motion.

### 3.5. Nonthermal Broadenings

The dynamics of the loops in unresolved scales are inferred from the Doppler width maps. The Doppler width  $\Delta\lambda_D$  of an optically thin line, after correcting for the instru-

mental broadening, is related to the temperature and non-thermal velocity,  $\xi$ , by the equation

$$v_D \equiv \frac{\Delta\lambda_D}{\lambda} c = \left( \frac{2kT_{\text{ion}}}{M_{\text{ion}}} + \xi^2 \right)^{1/2}, \quad (3)$$

where  $M_{\text{ion}}$  is the mass of the ion producing the line emission, and  $k$  is the Boltzmann constant. In the present study, the ion temperature,  $T_{\text{ion}}$ , is assumed to be equal to the electron temperature,  $T_e$ . This equation says that the non-thermal velocity,  $\xi$ , is the excess amount of an observed line width over the thermal contribution. The thermal contribution of a  $2.5 \times 10^4$  K plasma to the C II line,  $(2kT/M_{\text{ion}})^{1/2}$ , is  $5.8 \text{ km s}^{-1}$ , and that of a  $3.0 \times 10^5$  K plasma to the O VI line is  $17.6 \text{ km s}^{-1}$ . These values can be compared with the instrumental broadening of  $17.4 \text{ km s}^{-1}$ . Note that one should be cautious when using the O VI line for the measurement of nonthermal velocities, since the line profiles may be contaminated by the coronal background emission having a very broad line profile ( $v_D = 45 \text{ km s}^{-1}$ ). For this reason, we prefer the C II line, if available, for the determination of the nonthermal broadening. When using the O VI line, we should subtract the coronal background contamination before determining the line widths. The O VI line width map presented in Figure 6 has not been corrected for the coronal background.

Figure 6 shows that the line broadening appears to be very large at the two bright areas near the footpoints of loops 1, 2, and 3 in group I. This may represent a large nonthermal broadening, but we do not attempt to study these areas, since the detector is strongly saturated and it is hard to discriminate between true nonthermal broadenings and line broadenings caused by instrumental saturation. Consequently, our analysis of line broadenings is limited to

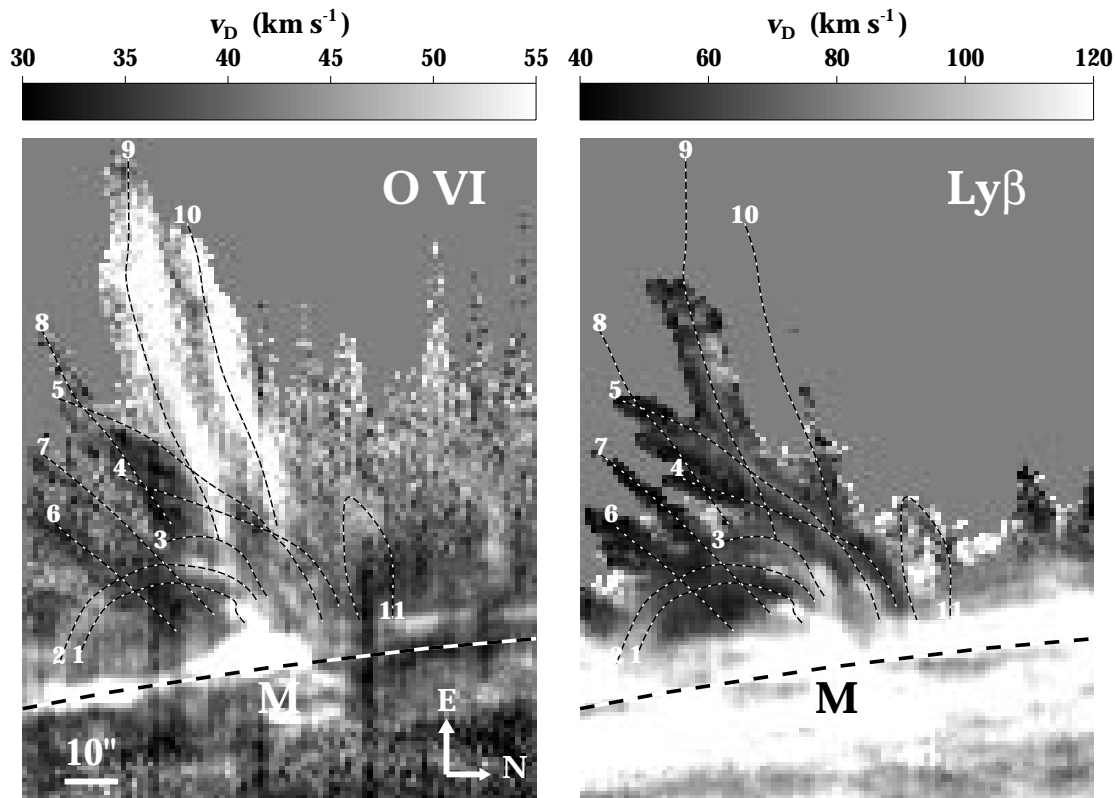


FIG. 6.—Doppler width maps of the active region in the O VI line (*left*) and the Ly $\beta$  line (*right*). The widths are corrected for the instrumental broadenings.

only the coronal portions of the loops, in which the effect of detector saturation is negligible.

At the coronal portions of group I loops, the Doppler broadening,  $v_D$ , ranges from 35–45 km s<sup>-1</sup> in the C II line. Central portions of these loops seem to show much lower values, but this is due to overlapping with loops 6 and 7, which belong to different groups. Figure 7 shows the typical C II line profile of loop 2 which is free from overlapping with loops from different groups. If we assume a temperature of

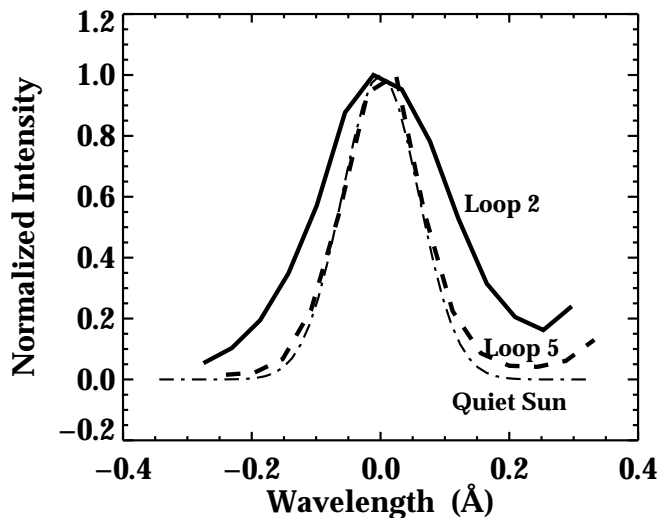


FIG. 7.—Typical C II  $\lambda 1037$  line profiles of loop 2 (group I) and loop 5 (group II) as compared with the computed average quiet Sun profile. The line center positions and peak intensities have been arbitrarily adjusted for an easy comparison of line widths.

10<sup>5</sup> K for these loops, the thermal contribution is 11.7 km s<sup>-1</sup>. Thus, we find that the thermal contribution to the line broadening is negligible in these loops, compared with nonthermal contribution  $\xi$ , which is found to be 33 to 43 km s<sup>-1</sup>. Note that the median value of the nonthermal broadening for the C II line, 38 km s<sup>-1</sup>, is much larger than the typical quiet Sun nonthermal broadening 16 km s<sup>-1</sup> (Chae et al. 1998a).

The loops belonging to groups II and III are found to have much smaller nonthermal broadenings than group I loops. Loops 4 and 5 in group II typically have  $v_D = 20$  km s<sup>-1</sup> in the C II line (see Fig. 7), which gives  $\xi = 19$  km s<sup>-1</sup> after correction for the thermal contribution of 7.1 km s<sup>-1</sup>. Loops 6, 7, and 8 in group III are hardly visible in the C II line, so here we have to use the O VI line. After correction of the contamination from the coronal background emission, we obtained  $v_D = 20$ –30 km s<sup>-1</sup> in this line, which results in  $\xi$  between 11 and 25 km s<sup>-1</sup> after subtracting the thermal contribution of 16.4 km s<sup>-1</sup>. Note that the median value, 18 km s<sup>-1</sup>, obtained for these loops are nearly the same as the typical value for group II loops, 19 km s<sup>-1</sup>, determined above.

Finally, loops 9 and 10 in group IV turn out to have the largest nonthermal broadenings. The Doppler broadening in the O VI line ranges from 50 to 63 km s<sup>-1</sup> after the coronal background emission has been subtracted. This means that  $\xi$  ranges from 47 to 60 km s<sup>-1</sup>. The residual coronal background emission arising from an imperfect correction may partly contribute to the line broadening, especially when the emission from the loop is highly shifted with respect to the coronal background emission. Therefore, it would be conservative to choose the smaller value of 47 km s<sup>-1</sup> as representative for the nonthermal broadening

in these loops. Note that this value is still much larger than any other nonthermal broadening velocity obtained above.

### 3.6. Spatial Relation to the X-Ray Flare

Our observations covered the decay phase of a B-class X-ray flare, allowing us to examine the spatial relationship between EUV loops/brightenings and the X-ray flare. Figure 8 presents a time sequence of *Yohkoh* Soft X-Ray Telescope (SXT) data taken with the AlMg filter and superposed on the corresponding Ly $\beta$  image of the active region. Note that the Ly $\beta$  image was constructed from the raster scan which lasted from 13:40 to 14:00 UT. The spatial resolution of the X-ray data is limited by the 5'' pixel size, so X-ray data do not show as fine structures as can be seen in the SUMER data. Nevertheless, they clearly reveal the evolution of the X-ray flare and its spatial relation to EUV loops.

During the evolution of the flare, two emission cores are seen in the X-ray intensity distribution: one near the area "M" and the other near the area "X". The core at "M" is cospatial with Ly $\beta$  brightenings, but the core at "X" has no corresponding brightening in Ly $\beta$ . The X-ray intensity at X begins to increase around 13:20 UT and reaches its peak around 13:35 UT. This temporal behavior is consistent with the *GOES* X-ray flux data presented in Figure 1. The X-ray intensity at M also reaches its peak around 13:35 UT, but it is much less than that at X. Therefore, it appears that the X-ray emission at X is mostly responsible for the X-ray flux of the flare. It is also likely that the origin of X-ray emission at M is somewhat different from that of the emission at X, since the region emits significantly in X-rays not only during the flare but also before and after the flare. The two bright X-ray cores at X and M are connected by X-ray emission bridges, and they may represent two different parts of the same X-ray loops. If so, the bright X-ray

source at M may be the footpoints of the X-ray loops at one side. On the other hand, the X-ray source at X is not likely to represent the footpoints at the other side, since it is located high above the limb, at about 9000 km. Neither does it seem to represent the tops of the loops. It appears that the X-ray source is located midway between the loop tops and the footpoints. In any case, it is interesting to note that the X-ray loops seen at 13:34 and 13:49 UT closely resemble the Ly $\beta$  loops that belong to group I. This indicates that group I loops are closely related to the X-ray flare.

## 4. SUMMARY AND DISCUSSION

Our results are summarized in Table 1. Based on the visibilities in different lines and on their morphology, 11 well-resolved loops have been classified into four groups. Typical values of length, diameter, temperature, density, bulk motion, and nonthermal velocity were determined in each of the groups. These values may be important observational constraints on theoretical modelings of active region loops. In several ways, our results may shed light on the structure and evolution of active region loops.

### 4.1. Thermal Structure of Magnetic Loops

Our results obviously support a notion that magnetic loops of temperatures below  $10^6$  K intrude into the surrounding corona with temperatures above  $10^6$  K. Moreover, we confirm that there exists loop-to-loop temperature variations at transition region temperatures with some loops being hotter than  $10^5$  K and others, not. The parts of a loop that are visible in the EUV lines we used may be regarded as isothermal with characteristic temperatures in the sense that temperature varies with a factor smaller than 2 or 3 and not by an order of magnitude. These results seem to be compatible with the view that the transition region is

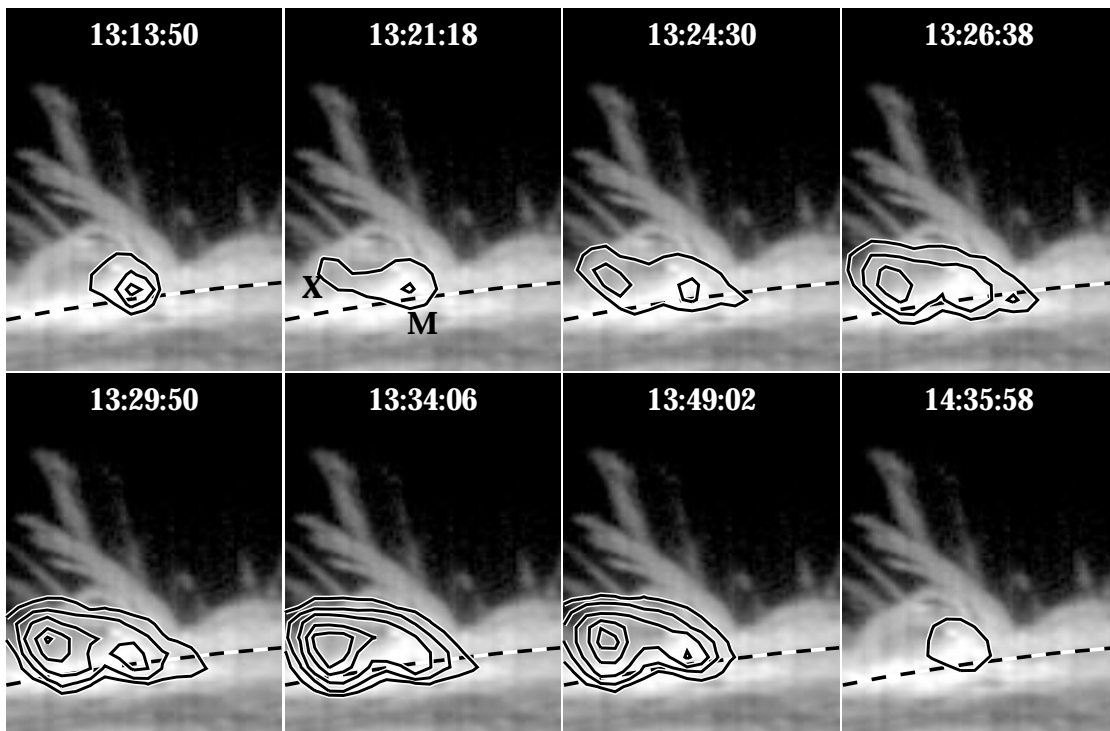


FIG. 8.—Time sequence of *Yohkoh* soft X-ray data (*contours*) superposed on the raster Ly $\beta$  image

TABLE 1  
LOOP CLASSIFICATION AND THEIR CHARACTERISTICS

Group	Loop Numbers	Properties	Typical Parameters
I.....	1, 2, 3, 11	Closed; visible in Ly $\beta$ , C II, and O VI; dynamic	$L = 5 \times 10^4$ km; $d = 1500$ km $s^{-1}$ ; $v_{los} \approx 20$ km $s^{-1}$ ; $\xi = 38$ km $s^{-1}$
II.....	4, 5	Open; visible in Ly $\beta$ and C II; quiet	$L > 12 \times 10^4$ km; $d = 1500$ km; $v_{los} \approx 0$ km $s^{-1}$ ; $\xi = 19$ km $s^{-1}$
III.....	6, 7, 8	Open/vertical; visible in O VI; quiet	$L > 12 \times 10^4$ km; $d = 1500$ km; $v_{los} \leq 10$ km $s^{-1}$ ; $\xi = 18$ km $s^{-1}$
IV.....	9, 10	Open/vertical; visible in O VI; very dynamic; rotational motions	$L > 16 \times 10^4$ km; $d = 2600$ km; $v_{los} = 25$ km $s^{-1}$ ; $\xi = 47$ km $s^{-1}$ ; $v_{rot} = 15\text{--}50$ km $s^{-1}$

a mixture of many isothermal loops with different temperatures. However, our observations also provide results that support the existence of nonnegligible temperature variations along the loops. First of all, the highest portion of many “open” loops are invisible in all of our EUV lines, implying that the temperature at that portion might be close to or hotter than  $10^6$  K. Even inside the portions that are visible in the lines, the relative visibilities in the different lines change with height, with the upper portions better visible in the O VI line, and the lower portions, in the C II and Ly $\beta$  lines. Our results thus indicate that both kinds of temperature variations exist in active region loops: variations from loop to loop and variations along each loop.

#### 4.2. Distinction between Stationary and Dynamic Loops

Our results show a clear distinction between stationary loops (groups II and III) and dynamic loops (groups I and IV). The dynamic loops are characterized by large bulk motions,  $v = 20$  km  $s^{-1}$ , and large nonthermal motions,  $\xi = 40\text{--}50$  km  $s^{-1}$ , whereas stationary loops have small bulk motions,  $v < 10$  km  $s^{-1}$ , and small nonthermal motions,  $\xi = 20$  km  $s^{-1}$ . Figure 9 clearly illustrates this distinction based on a comparison of the O VI profiles of a stationary loop (loop 5) and a dynamic loop (loop 9). This distinction may provide a way to resolve the contradicting results on the measurements of nonthermal broadenings in active regions. Many studies have produced the result that the nonthermal broadening,  $\xi$ , measured at coronal temperatures are  $10\text{--}20$  km  $s^{-1}$  both in active regions and in the quiet Sun (e.g., Cheng, Doschek, & Feldman 1979; Chae

et al. 1998a; Hara & Ichimoto 1999). On the other hand, the measurements by the Flat Crystal Spectrometer (FCS) aboard the *Solar Maximum Mission* (SMM) produced larger values of  $40\text{--}60$  km  $s^{-1}$  (Saba & Strong 1991; Antonucci & Doderer 1995). From one data set with SUMER, we obtained both small nonthermal broadening values (i.e., about  $20$  km  $s^{-1}$  in stationary loops) and large values (i.e., about  $50$  km  $s^{-1}$  in dynamic loops). Therefore, the studies that reported large values might have measured dynamic loops, whereas other studies that reported smaller values might have measured stationary loops.

It appears that the dynamic loops in groups I and IV are related to the B-class flare. Comparison with *Yohkoh* SXT data showed that the X-ray loops resemble the dynamic loops in group I seen in the O VI and Ly $\beta$  lines. This correlation between O VI and Ly $\beta$  emission and X-ray emission may be the result of thermal evolution of the magnetic loops either due to heating (EUV loops evolving into X-ray loops) or cooling (X-ray loops evolving into EUV loops). The dynamic loops in group IV may be undergoing eruption during the flare, as the open and vertical shapes and large bulk motions suggest. *Yohkoh* soft X-ray observations have shown that loop eruptions are commonly associated with flares, not only in long-duration events (Tsuneta et al. 1992; Hanaoka et al. 1994) but also in impulsive compact-loop flares (Shibata et al. 1995; Ohyama & Shibata 1998).

#### 4.3. Physical Nature of Nonthermal Broadening

Our observations provide a couple of important results to help in understanding the physical nature of nonthermal motions. First, we confirm that nonthermal motions persist even in spatially resolved loops. Our observations indicate that nonthermal broadening comes from unresolved motions with spatial scales much smaller than the loop diameters, and timescales shorter than the exposure time, 7 s. This demonstrates that nonthermal motions are not the result of superposition of many loops. Instead, nonthermal motions seem to be an intrinsic property that characterizes each individual loop, just as temperature does. Moreover, large nonthermal motions are associated with large bulk motions. This suggests a strong coupling between bulk motions and nonthermal broadenings.

If nonthermal broadenings were caused by a superposition of laminar flows within a loop, the loop should have a filamentary structure with many threads with different velocities along the field lines. If nonthermal broadenings were due to waves, they should have very short wavelengths and periods. However, for both possibilities, it is not easy to explain the isotropic nature of nonthermal broadenings (e.g., Chae et al. 1998a; Hara & Ichimoto 1999). We prefer to interpret the nonthermal broadenings as the result of MHD turbulence, since turbulence successfully fits the small-scale and isotropic nature of nonthermal

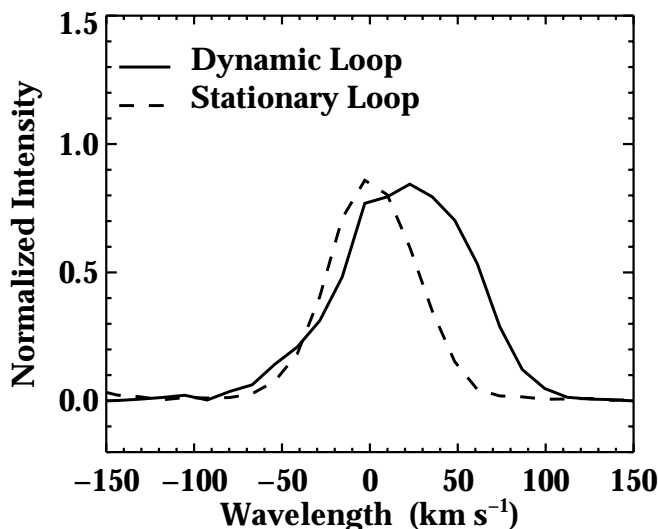


FIG. 9.—Typical O VI  $\lambda 1038$  line profiles of stationary and dynamic loops, respectively. The coronal background line emission has been subtracted from the profiles.

broadening. The inferred coupling between bulk motions and nonthermal broadenings is also consistent with the possibility that the turbulence is powered by bulk motions through cascading down of mechanical energy. As demonstrated by Dmitruk & Gómez (1997), the MHD turbulence inside loops may be closely connected to topological relaxation which has been proposed as a mechanism of nano-flares (e.g., Parker 1988). Consequently, we postulate that when loops erupt or are dynamically perturbed in other ways, some of the mechanical energy in bulk motion and magnetic field cascade down to turbulent kinetic and magnetic energy which will eventually be dissipated as heat and radiation. One would expect that bulk motions with large velocity shear and magnetic fields with large magnetic shear can easily cascade down to turbulent energy.

#### 4.4. Large Velocity Shears: Rotational Motions?

An interesting finding is that some dynamic loops display large velocity shears with the sign of line-of-sight velocity changing across the loops. This kind of motions have been also reported in spicules (e.g., Beckers 1972), in macrospicules (Pike & Harrison 1997; Pike & Mason 1998), and in H $\alpha$  surges (Canfield et al. 1996). Thus, it appears that they are quite frequent in erupting structures. So far, there is no unambiguous interpretation of the observed velocity shears in different lines. They may either represent the rotational motions around loop axes or may be the effect of the overlapping of two adjacent loops with large line-of-sight velocities in opposite directions. We think that the velocity shears are probably caused by rotational motion. If so, the existence of an azimuthal magnetic field component that encircles the axis may be required to guide the rotational motion. The low limit of the azimuthal field strength,  $B_\phi$ , may be obtained from the equipartition assumption between kinetic energy and magnetic energy  $\rho v_{\text{rot}}^2/2 \approx B_\phi^2/8\pi$ , where  $\rho$  is the mass density. It then follows that  $B_\phi \approx (4\pi\rho)^{1/2}v_{\text{rot}}$ . Assuming  $n_e$  in the range  $10^9$ – $10^{10}$  cm $^{-3}$  and  $v_{\text{rot}} = 50$  km s $^{-1}$ , we get an low limit estimate  $B_\phi \approx 0.6$ – $1.9$  G. Consider-

ing the possibility that the observed rotational velocity might have been underestimated owing to projection and that the field might be guiding the flows in a rigid fashion, it appears that the required azimuthal field strength should be even higher than a few Gauss.

We postulate that rotational motions and magnetic twist may be a good energy source for coronal heating. Under the assumptions that radiative losses are neglected and that there is an equipartition between kinetic energy and azimuthal magnetic energy, we can roughly estimate the amount of temperature increase due to the dissipation of the two kinds of mechanical energy:

$$\Delta T \approx \frac{2\mu m_H v_{\text{rot}}^2}{3k} = 5 \times 10^5 \left( \frac{v_{\text{rot}}}{100 \text{ km s}^{-1}} \right)^{1/2} \text{ K}, \quad (4)$$

where  $\mu$  is the mean molecular weight, and  $m_H$  is the mass of a hydrogen atom. The equation shows that a cool loop having an initial rotational motion of 100 km s $^{-1}$  can be heated to an upper transition region temperature. Note that we have assumed in situ heating and have not considered radiative cooling. When radiative losses are considered, the heating timescale needs to be shorter than the radiative cooling timescale so that a cooler loop can evolve into a hotter one. This point could be resolved when temperature and electron density are properly determined.

We are grateful to the anonymous referee for his comments, which greatly helped in improving the paper. We are indebted to T. Moran, H. Warren, and D. Zarro for discussions. The *Yohkoh* soft X-ray data used in the present work were kindly provided by the Solar Data Analysis Center at NASA Goddard Space Flight Center. This work is partially supported by NSF under grant ATM 97-14796 and by NASA under grants NAG 5-4919, NAG 5-7349, and NAG 5-7350 to BBSO. The SUMER project is financially supported by DLR, CNES, NASA, and the ESA PRODEX programme (Swiss contribution).

#### REFERENCES

- Antonucci, E., & Dodero, M. A. 1995, *ApJ*, 438, 480  
 Arnaud, M., & Rothenflug, R. 1985, *A&AS*, 60, 425  
 Beckers, J. M. 1972, *ARA&A*, 10, 73  
 Brekke, P. 1998, in *ASP Conf. Ser.* 155, Three-Dimensional Structure of Solar Active Regions, ed. C. E. Alissandrakis & B. Schmieder (San Francisco: ASP), 150  
 Brekke, P., Kjeldseth-Moe, O., & Harrison, R. A. 1997, *Sol. Phys.*, 175, 511  
 Canfield, R. C., Reardon, K. P., Leka, K. D., Shibata, K., Yokoyama, T., & Shimojo, M. 1996, *ApJ*, 464, 1016  
 Chae, J., Schühle, U., & Lemaire, P. 1998a, *ApJ*, 505, 957  
 Chae, J., Yun, H. S., & Poland, A. I. 1998b, *ApJS*, 114, 151  
 Cheng, C.-C., Doschek, G. A., & Feldman, U. 1979, *ApJ*, 227, 1037  
 Dmitruk, P., & Gómez, D. O. 1997, *ApJ*, 484, L83  
 Fludra, A., Brekke, P., Harrison, R. A., Mason, H. E., Pike, C. D., Thompson, W. T., & Young, P. R. 1997, *Sol. Phys.*, 175, 487  
 Hanaoka, Y., et al. 1994, *PASJ*, 46, 205  
 Hara, H., & Ichimoto, K. 1999, *ApJ*, 513, 969  
 Kjeldseth-Moe, O., & Brekke, P. 1998, *Sol. Phys.*, 182, 73  
 Lemaire, P., et al. 1997, *Sol. Phys.*, 170, 105  
 Matthews, S. A., & Harra-Murnion, L. K. 1997, *Sol. Phys.*, 175, 541  
 Ohya, M., & Shibata, K. 1998, *ApJ*, 499, 934  
 Parker, E. N. 1988, *ApJ*, 330, 474  
 Pike, C. D., & Harrison, R. A. 1997, *Sol. Phys.*, 175, 457  
 Pike, C. D., & Mason, H. E. 1998, *Sol. Phys.*, 182, 333  
 Saba, J. R., & Strong, K. T. 1991, *ApJ*, 375, 789  
 Shibata, K., Masuda, S., Shimojo, M., Hara, H., Yokoyama, T., Tsuneta, S., Kosugi, T., & Ogawara, Y. 1995, *ApJ*, 451, L83  
 Tsuneta, S., Takahashi, T., Acton, L. W., Bruner, M. E., Harvey, K., & Ogawara, Y. 1992, *PASJ*, 44, L211  
 Uchida, Y., et al. 1992, *PASJ*, 44, L155  
 Wilhelm, K., et al. 1995, *Sol. Phys.*, 162, 189  
 ———. 1997, *Sol. Phys.*, 170, 75